

# Optical characterization of multilayer $\alpha$ -In<sub>2</sub>Se<sub>3</sub>

Yujin Cho,<sup>1</sup> Sean M. Anderson,<sup>2,\*</sup> Bernardo S. Mendoza,<sup>2</sup> Shun Okano,<sup>3</sup> N. Arzate,<sup>2</sup> Anatoli I. Shkrebtii,<sup>4</sup> Di Wu,<sup>1</sup> Keji Lai,<sup>1</sup> Ramón Carriles,<sup>2</sup> D. R. T. Zahn,<sup>3</sup> and M. C. Downer<sup>1</sup>

<sup>1</sup>*Department of Physics, University of Texas at Austin, Austin, Texas 78712, USA*

<sup>2</sup>*Centro de Investigaciones en Óptica, León, Guanajuato 36000, México*

<sup>3</sup>*Semiconductor Physics, Chemnitz University of Technology, 09107, Chemnitz, Germany*

<sup>4</sup>*Ontario Tech University, Oshawa, ON, L1G 0C5, Canada*

(Dated: December 3, 2019)

Ferroelectric materials possess spontaneous electric polarization below the phase transition temperatures, which are switchable with an external electric field. 2D ferroelectric materials have many potential uses, but an understanding of how this spontaneous ferroelectricity changes with different physical properties is crucial to properly engineer these materials for future applications. These properties can be effectively probed using optical techniques, which is excellent motivation for carrying out a systematic study of various opto-electronic properties using spectroscopic techniques. In particular, this work focuses on the evolution of the linear and nonlinear optical responses of layered and bulk  $\alpha$ -In<sub>2</sub>Se<sub>3</sub> for different nano-flake thicknesses and orientations, using high-resolution spectroscopic measurements and *ab initio* density functional theory (DFT) and time-domain DFT (TDDFT) calculations.

Nonlinear second-harmonic generation (SHG) spectroscopy measurements feature a broad resonant peak centered around 1.4 eV. The intensity of the SHG spectra increases with the number of layers up to three quintuple layers, and then steadily decreases for larger numbers. With support from DFT calculations, we found that the net ferroelectric polarization on 2 QLs is most likely zero, while thicker QLs have non-zero polarization. We also present transmission measurements for layered samples over a photon energy range of 1.5–4 eV, along with ellipsometry data for the complex index of refraction for bulk  $\alpha$ -In<sub>2</sub>Se<sub>3</sub>; these are all compared with *ab initio* DFT and TDDFT calculations. The linear response is not as sensitive to structural variations as the SHG spectra, but allow us to discern critical point transitions and to extract the optical band gap values, that are also corroborated with  $G_0W_0$  calculations. The thorough study of the linear and nonlinear optical properties of  $\alpha$ -In<sub>2</sub>Se<sub>3</sub> will be useful for potential applications as optoelectronic devices.

## I. INTRODUCTION

III-VI semiconductor materials exhibit a variety of structural and electronic properties, due mostly to the complex nature of the valence electrons in the group VI elements. These compound materials demonstrate a rich variety of compositions. Among numerous bulk III-VI crystals, recent findings show that these materials also exist in the form of two-dimensional (2D) hexagonal nanofilms that are only a few atoms thick<sup>1–3</sup>. In particular, III<sub>2</sub>-VI<sub>3</sub> compounds (also known as A<sub>2</sub>B<sub>3</sub>-type chalcogenides) composed of indium (In) and selenium (Se) can form several single-phase and layered In-Se compounds; namely, InSe<sup>4</sup>, In<sub>2</sub>Se<sub>3</sub>, In<sub>3</sub>Se<sub>4</sub><sup>5,6</sup> and In<sub>4</sub>Se<sub>3</sub>, all of which have been obtained experimentally<sup>7–9</sup>.

The switchability of ferroelectric polarization below the transition temperature<sup>10</sup> is desirable for many applications<sup>11</sup>, and particularly useful for storing information in memory devices at higher speeds with less power consumption<sup>12–14</sup>. In addition, a growing interest in device miniaturization naturally leads to search for new thin film ferroelectrics<sup>15,16</sup>. However, when the thickness shrinks beyond some critical value, usually on the order of a few nanometers, strong depolarization fields tend to suppress the ferroelectricity; this has been a significant challenge for traditional perovskite thin films<sup>17,18</sup>. The strain effect induced at the interface

between the substrate and the film affects the spontaneous polarization near the interface<sup>19,20</sup>. Fortunately, 2D ferroelectrics can potentially overcome these difficulties. Lack of out-of-plane chemical bonding of 2D materials reduces misfit strain at the interface between the substrate and the films<sup>21</sup> and the spontaneous polarization remains switchable at a few layers. In-plane ferroelectricity of 2D materials has been demonstrated in several materials such as MoS<sub>2</sub>, SnTe, and Phosphorene analogues<sup>21–23</sup>.

Layered In<sub>2</sub>Se<sub>3</sub> is a 2D van der Waals (vdW), nonplanar, and quasi-two-dimensional semiconducting material<sup>24</sup> that has recently garnered significant interest with a large variety of identified applications<sup>1–3,25,26</sup>. It has several advantageous optoelectronic properties; for instance,  $\alpha$ -In<sub>2</sub>Se<sub>3</sub> demonstrates a thickness-dependent band gap<sup>27</sup> which enables tuning of its dielectric function, and thus, optical properties<sup>28,29</sup>. It is also temperature tunable: non-centrosymmetric  $\alpha$ -In<sub>2</sub>Se<sub>3</sub> transforms into centrosymmetric  $\beta$ -In<sub>2</sub>Se<sub>3</sub> at 475 K<sup>30</sup>, which is propitious for phase-change memory applications<sup>31,32</sup>.

In contrast to the single-atomic graphene-like materials, or the more complex phosphorene and MoS<sub>2</sub>, the basic In<sub>2</sub>Se<sub>3</sub> layer consists of five alternating Se and In atoms that form the so-called quintuple layer (QL). Numerous structural variations of the QLs are possible<sup>10</sup>, with the two most energetically stable layered structures belong to the  $\alpha$  and  $\beta$  phases. Both are semiconducting

with an energy bandgap in the optical range, with widely varying reported experimental and theoretical bandgap values. The  $\alpha$  phase has the lowest total energy and belongs to the  $R3m$  space group; in contrast, the  $\beta$  phase is less energetically stable and belongs to the  $R\bar{3}m$  space group. Recent experimental work has demonstrated that  $\alpha$ -In<sub>2</sub>Se<sub>3</sub> possesses room-temperature out-of-plane ferroelectricity down to thicknesses of a few layers<sup>14,33–36</sup>, and expected to persist even down to a single QL<sup>10</sup>. However, the presence of a strong dipole moment favors the formation of 2D domains with opposite dipole orientations which reduces the electrostatic energy; for instance, the potential barrier for changing the dipole orientation is around 0.07 eV<sup>10</sup>. Experimental results<sup>14</sup> indicate that a few volts of applied electric potential in the perpendicular direction can switch the dipole directions of the QLs. Moreover, the magnitude of the spontaneous polarization is not linear to the thickness; it is expected to be maximized at three QLs, and decreases with additional layers<sup>10</sup>. Multi-QL systems have weak-vdW bonded layers, and so we must consider several QL orientations with parallel and opposite dipole moments<sup>14,28,33</sup>. Since the experimentally observed symmetry for single and multiple QLs at room temperature is consistent with the  $R3m$  space group<sup>14,28</sup>, we will focus exclusively on the optical characterization of  $\alpha$ -In<sub>2</sub>Se<sub>3</sub> as a promising ferroelectric material.

We can gain a critical understanding of this material from its optical properties; for instance, the transmission and absorption spectra are directly related to different intrinsic quantities such as the dielectric function and the electronic band structure. Likewise, optical second-harmonic generation (SHG) is an efficient and non-destructive spectroscopic method, that is very sensitive to even small changes in the atomic structure and symmetry properties (including centrosymmetry). SHG could allow us to characterize the polarization dependence of the optical response, and potentially elucidate information about the microscopic structure of the individual QLs. These quantities can be explored experimentally using spectroscopic methods, and theoretically determined from *ab initio* calculations. Knowledge of how the spontaneous polarization changes with the thickness and microscopic arrangement of this material is crucial for engineering  $\alpha$ -In<sub>2</sub>Se<sub>3</sub> towards device applications; therefore, this is excellent motivation for carrying out a systematic study of various opto-electronic properties of  $\alpha$ -In<sub>2</sub>Se<sub>3</sub>, using several experimental and theoretical spectroscopic techniques. In particular, this work focuses on the evolution of the linear and nonlinear optical responses of layered and bulk  $\alpha$ -In<sub>2</sub>Se<sub>3</sub> for different nano-flake thicknesses and orientations. The results presented from high-resolution spectroscopic measurements are complemented by *ab initio* calculations that allow insight into the intrinsic opto-electronic properties of the material, to elucidate the ferroelectric nature and microscopic characteristics.

This paper is organized as follows. In section II, we

present the experimental and computational methods used to carry out the study of the optical properties of  $\alpha$ -In<sub>2</sub>Se<sub>3</sub>. In section III, we present our measured and calculated spectra for both the layered and the bulk material, obtained from direct spectroscopic measurements and *ab initio* calculations. Lastly, we list our conclusions and final remarks in section IV.

## II. METHODS

### A. Experimental Methods

The In<sub>2</sub>Se<sub>3</sub> nano-flakes were grown on fluorophlogopite mica substrates by vapor phase deposition (VPD), which provides highly crystalline samples and well-controlled thickness profiles<sup>28,33,37,38</sup>. The flakes were synthesized by vdW epitaxy in a 1-inch diameter horizontal quartz tube furnace (Lindberg Blue M HTF55667C). Bulk In<sub>2</sub>Se<sub>3</sub> powder (99.99 %, Alfa Aesar) was placed at the center and heated to 740 °C. The vapor flowed downstream with 30–200 SCCM argon gas at 20 Torr and deposited on mica substrates, placed 7–12 cm away from the heated center, forming layered In<sub>2</sub>Se<sub>3</sub> flakes, typically a few tens of microns wide. After 10 minutes, the tube was cooled down to room temperature at a rate slower than 5 °C/min. Like most 2D materials, In<sub>2</sub>Se<sub>3</sub> has a hexagonal structure that deposits in triangular flakes, except for single quintuple layer flakes, which instead form rounded shapes on the mica substrate (see Figures 1a and 1b). We confirmed the thickness and the crystallinity of the layers using atomic force microscopy and SHG microscopy, verifying the presence of the  $\alpha$ -phase of In<sub>2</sub>Se<sub>3</sub> with rotational anisotropic SHG (RASHG) microscopy. This method has been previously used with success to synthesize  $\alpha$ -In<sub>2</sub>Se<sub>3</sub>, having been confirmed by transmission electron microscopy<sup>28</sup>.

Optical transmission spectroscopy was performed on a micro-imaging ellipsometer Nanofilm EP4 (Accurion GmbH), equipped with a Xenon arc lamp with a wavelength range from 950–250 nm (photon energy 1.3 eV to 4.96 eV, respectively), at normal incidence. A single diffraction grating produced a monochromatic incident light. Reflected light was collected and imaged with  $\sim 1 \mu\text{m}$  spatial resolution to an array with a Nikon 50 $\times$  long working distance microscope objective (N.A. = 0.45), enabling signals reflected from within the boundaries of a single tens-of-micron-sized flake to be analyzed. For the SHG spectroscopy, we used a Ti:Sapphire laser (Coherent Chameleon Vision II) operating at an 80 MHz repetition rate with 140 fs pulse duration. The wavelength of the laser was tunable from 680 nm to 1040 nm. The laser light is incident on the sample at 45° and the beam spot size was around 3  $\mu\text{m}$ . We normalized the measured SHG intensity from  $\alpha$ -In<sub>2</sub>Se<sub>3</sub> to that of  $\alpha$ -quartz to better estimate the magnitude of the  $\chi^{(2)}$  tensor components. A  $\lambda/2$ -waveplate and a linear polarizer were used to select incoming polarization and SHG polariza-

tion, respectively. All measurements presented here were checked for consistency by collecting data from several regions on the same sample, as well as from different flakes with the same number of QLs.

## B. Computational methods

We relaxed the atomic positions for each QL variant using the repeated slab approach with the Quantum Espresso<sup>39</sup> software package, within the DFT-LDA framework with plane-waves and pseudopotentials using a 60 Ry cutoff. Single QLs of either structure belong to the  $R3m$  space group with a lattice constant of  $a = 4.106 \text{ \AA}$ <sup>10</sup>. We modeled several weakly vdW-bonded multi-QL configurations to determine the optimal interlayer distances and QL stacking arrangements. In agreement with previous calculations<sup>10,14,28</sup>, we found that the most energetically stable configuration is an ABC QL stacking<sup>10</sup> with an inter-QL separation of 2.95 Å. This separation, as well as the atomic structure of the multi-QL systems, does not depend on the dipole orientation of the individual QLs within the stack.

The calculation of the nonlinear susceptibility tensor  $\chi(-2\omega; \omega, \omega)$  and the dielectric functions for layered  $\alpha\text{-In}_2\text{Se}_3$  were carried out with the TINIBA code<sup>40</sup> within the independent-particle DFT-LDA framework<sup>41</sup>. First, we calculated the electronic wave-functions using the ABINIT code<sup>42,43</sup> with a planewave basis set with an energy cutoff between 20 to 40 Hartree, and Troullier-Martins LDA pseudopotentials<sup>44</sup>. The spectra were properly converged with several thousand  $\mathbf{k}$ -points in the IBZ. The contribution from the nonlocal part of the pseudopotentials was carried out using the DP code<sup>45,46</sup> with a basis set of at least 5000 planewaves. The total number of bands included in the calculation was at least  $12(N + 1)$ , where  $N$  is the total number of QLs. We included a vacuum region between 30 to 130 Å (depending on the number of QLs) to compensate for the net dipole moment present in some stacking arrangements and to avoid spurious wave-function tunneling. All results presented below are thus normalized to the vacuum region included in the total supercell height<sup>47</sup>; yielding consistent results regardless of vacuum region size. The components of  $\chi(-2\omega; \omega, \omega)$  are also properly normalized to obtain the correct surface units of  $\text{pm}^2/\text{V}$ . Quasiparticle effects are included, when pertinent, via a rigid scissors approach.

The calculation of the dielectric function for bulk  $\alpha\text{-In}_2\text{Se}_3$  was carried out within the TDDFT framework using the DP<sup>45,46</sup> code, where the independent-particle response function was constructed using Kohn Sham (KS) orbitals, within the random phase approximation (RPA) including local-field effects. The electronic wave-functions were calculated using the ABINIT code<sup>42,43</sup> and a planewave basis set with an energy cutoff of 15 Hartrees and Troullier-Martins LDA pseudopotentials<sup>44</sup>, and at least 1700  $\mathbf{k}$ -points in the irreducible Brillouin

zone (IBZ) with 18 unoccupied states (30 total).

Lastly, we carried out  $G_0W_0$ <sup>48</sup> calculations in order to obtain self-corrected band gap values at the  $\Gamma$  point. These were carried out using the ABINIT code<sup>42,43</sup> using similar parameters to those described above. We obtained values for 1 QL, 2 QLs, and bulk. These values were used to adjust the required eigen-energies via a rigid scissors approach for the different spectroscopic calculations above.

## III. RESULTS

### A. RASHG and SHG Spectroscopy

Figures 1a and 1b show optical images of two  $\alpha\text{-In}_2\text{Se}_3$  flakes. Each QL is around 0.84 nm thick, verified via atomic force microscopy. Due to the low absorption of 1 QL and the weak optical contrast between the flakes and the mica substrate, it was difficult to image the 1 QL regions with a normal optical microscope. Since the visible light absorption increases linearly with the thickness, larger QL stacks have better optical contrast, as can be seen from the small center triangle with 5 QL in Figure 1b.

Figures 1c and 1d show SHG micrographs taken at a fundamental wavelength of 780 nm (1.59 eV), for the two samples shown in Figures 1a and 1b, respectively. The mica substrate is centrosymmetric, so we expect a strong SHG response only from the  $\alpha\text{-In}_2\text{Se}_3$  nanoflakes that are non-centrosymmetric at room temperature. This provides better contrast between the sample and the substrate. In Figures 1c and 1d, we measured *s*-polarized SHG light generated by *s*-polarized incident electric fields. We kept the laser intensity below 2 mW to avoid laser-induced charge or damaging the sample. At this laser intensity, the SHG response from 1 QL is very close to the background intensity. The SHG response increases sharply from 1 QL to 2 QL; 3 QL has only a slightly higher response than 2 QL. Note that the SHG intensity from 5 QL (small center triangle in Figure 1d) is lower than that of 3 QL.

For ease of notation, let us denote the incoming  $1\omega$  photon polarization as either *p* or *s*, and analogously, the outgoing  $2\omega$  photon polarization with either capital *P* or *S*. To elucidate the horizontal stacking order of the two samples, we used the RASHG technique to measure SHG intensity with *sS* polarization while rotating the sample. RASHG is useful to confirm the relative crystallographic orientation between QLs, as well as the symmetry relations (and thus space group) of the material. We used a higher laser power to obtain a strong SHG response from 1 QL. We kept the laser beam at one spot for no more than a second to avoid the spurious laser induced effects. The  $R3m$  space group has four independent nonzero components of the nonlinear susceptibility tensor,  $\chi^{xxx} = \chi^{xxy} = \chi^{xyx} = \chi^{xxz} = \chi^{yyz}$ ,  $\chi^{zxx} = \chi^{zyy}$ , and  $\chi^{zzz}$ <sup>49,50</sup>. From these components,

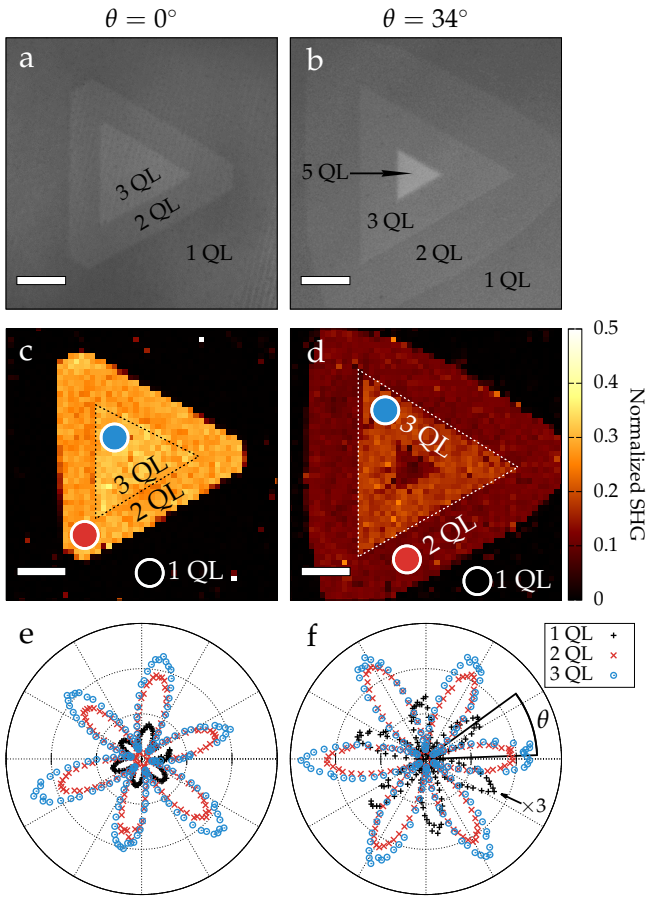


FIG. 1. **a–b**, optical images of two  $\alpha$ -In<sub>2</sub>Se<sub>3</sub> samples used in this work. **c–d**, SHG micrographs of the same samples. The white bars represent 50  $\mu$ m.. The number of QLs are labeled in the appropriate regions. **e–f**, RASHG patterns measured from the samples; line colors correspond to the colored dots in **c** and **d**.  $\theta$  is the relative angle of crystallographic orientation between QLs. SHG measurements (**c–f**) where taken at a fundamental wavelength of 780 nm (1.59 eV).

we can fit the expected RASHG patterns and determine the relative crystallographic orientation between different QLs. We can isolate two tensor components,  $\chi^{xxx}$  and  $\chi^{zxx}$ , whose mirror plane is perpendicular to the  $y$ -axis, by selecting  $sS$  and  $sP$  polarization combinations. For these polarization configurations, the outgoing SHG fields are related to the incoming fields as<sup>51,52</sup>,

$$E_S(2\omega) = [A' \sin 3\phi \chi^{xxx}] E_s^2(\omega),$$

$$E_P(2\omega) = [A \chi^{zxx} + B \sin 3(\phi + \theta) \chi^{xxx}] E_s^2(\omega),$$

where  $A$ ,  $B$ , and  $A'$  are fitting parameters,  $\phi$  is the azimuthal angle and  $\theta$  is the relative angle between QLs.  $E_s(\omega)$  is the electric field taken at a fundamental frequency  $\omega$  that is incident on the samples. We can readily see that  $sS$  polarized SHG requires only  $\chi^{xxx}$ , while  $sP$  polarized SHG depends on  $\chi^{xxx}$  and  $\chi^{zxx}$ .

From these relations, we can determine the relative

crystallographic orientation between QLs. For the sample shown on the left side of Figure 1 (a, c, and e), all QLs are oriented along the same direction. On the other hand, the sample shown on the right side of Figure 1 (b, d, and f), has its 1 QL region rotated by 34° with respect to the overlaying QLs. As seen in Figure 1f, the maxima of the 1 QL RASHG values (black crosses) fall between the maxima of the 2 QL (red exes) and 3 QL (blue circles). From this point on, we will refer the left sample as  $\theta = 0^\circ$  (also known as AB stacking order), the right sample as  $\theta = 34^\circ$ . We verified the crystallographic orientation of more than 15 other nano-flakes on the same substrate, with all of them having either a value of  $\theta = 0^\circ$  or  $\theta = 180^\circ$ ; these samples are even discernible via conventional optical microscopy.

Although  $\theta = 34^\circ$  is not a preferred stacking orientation, it is possible that a defect on the first QL acted as a seed for the next layers during the growth process, which made it grow at a random crystallographic orientation. It is clear from Figures 1c and 1d that this stacking angle strongly affects the SHG responses; the overall SHG intensity of  $\theta = 34^\circ$  at 780 nm is weaker by a factor of three compared to  $\theta = 0^\circ$  for both  $sS$  and  $sP$  SHG polarizations. Similar trends have been observed on artificially stacked MoS<sub>2</sub> layers; the Raman, SHG, and photoluminescence spectra were greatly affected by the horizontal stacking orientation due to changes in the interlayer coupling<sup>53</sup>. Therefore, we can expect that the interlayer distance between 1 and 2 QL is larger when  $\theta = 34^\circ$  than the interlayer distance for  $\theta = 0^\circ$ , which leads to a weaker interlayer coupling.

To observe the spectroscopic SHG response, we varied the fundamental wavelength from 1.2 to 1.7 eV (730 to 1040 nm). We fixed the azimuthal angle to a maximum in the RASHG measurement for each polarization configuration of Figure 1. Figures 2a–2d presents the SHG spectra measured for  $sP$  and  $sS$  polarizations for both  $\theta = 0^\circ$  and  $\theta = 34^\circ$  samples. Both samples present a broad resonance around 1.4 eV originating from a resonant optical transition around the  $\Gamma$  point, with  $sP$  polarization yielding a more intense SHG response than  $sS$ . For  $\theta = 0^\circ$ , the  $sP$  SHG intensity around 1.4 eV is around twice as large as the  $sS$  intensity, and  $\theta = 0^\circ$  is 3 times more intense than  $\theta = 34^\circ$  for  $sP$  polarization, and around 2 times more for  $sS$  polarization. Although 1 QL appears very small, we know from Figure 1 that 2 QL response is around 5 times more intense. 3 QL intensity is around 25% (18%) more intense than 2 QL for  $\theta = 0^\circ$  ( $\theta = 34^\circ$ ). Figure 2e presents the normalized SHG intensity as a function the number of QLs at 1.59 eV. We normalized the intensity with respect to the 2 QL response. Above 3 QLs, the SHG intensity decreases as the number of layers increases. This experimentally validates that the net polarization (electric dipole) does not increase monotonically with the number of QLs; instead, some amount of out-of-plane polarization is canceled out due to charge transfer, generating opposite polarization across the film<sup>10</sup>. From those two samples, it is clear that

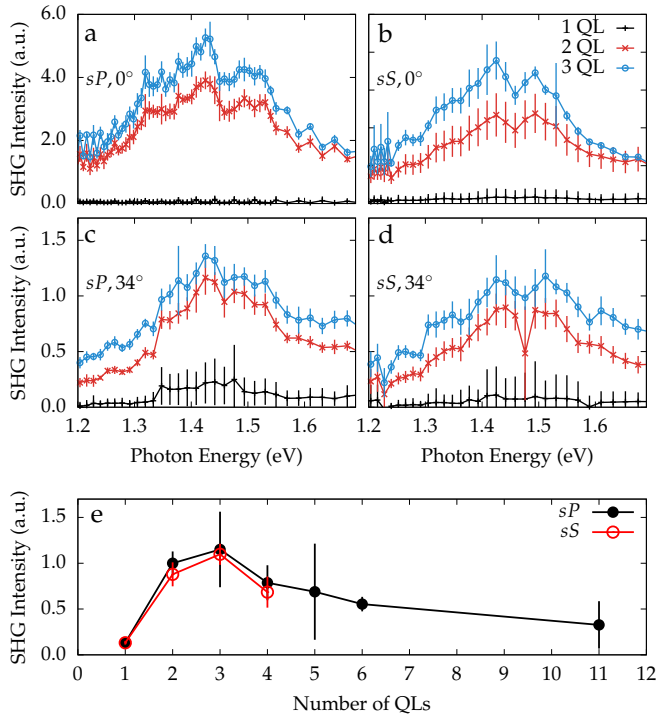


FIG. 2. Normalized SHG intensity for: **a**,  $sP$  polarization for the  $\theta = 0^\circ$  sample; **b**,  $sS$  polarization for the  $\theta = 0^\circ$  sample; **c**  $sP$  polarization for the  $\theta = 34^\circ$  sample; and, **c**  $sS$  polarization for the  $\theta = 34^\circ$ . **e**, normalized SHG intensity as a function of the number of layers, measured at 780 nm (1.59 eV) fundamental wavelength for  $sP$  and  $sS$  polarizations for the  $\theta = 0^\circ$  sample. All SHG intensities were normalized against  $\alpha$ -quartz.

the SHG response of  $\alpha$ -In<sub>2</sub>Se<sub>3</sub> has not only thickness dependence but is also highly sensitive to the horizontal stacking arrangement.

As shown previously, s-in/s-out SHG intensity depends on one nonlinear tensor component,  $\chi_{xxx}^{(2\omega)}$ , and s-in/p-out depends on  $\chi_{xxx}^{(2\omega)}$  and  $\chi_{zxx}^{(2\omega)}$ . Thus, we calculated  $\chi_{xxx}^{(2\omega)}$  from s-in/s-out SHG intensity and estimated  $\chi_{zxx}^{(2\omega)}$  using  $\chi_{xxx}^{(2\omega)}$ . The equations can be rewritten as:

$$|\chi_{xxx}^{(2\omega)}| = \sqrt{I_{sS}} \frac{1}{A'} \frac{E^Q}{E_s^2}, \quad (1)$$

$$|\chi_{zxx}^{(2\omega)}| = \sqrt{I_{sP}} \frac{1}{A} \frac{E^Q}{E_s^2} - \frac{B}{A} |\chi_{xxx}^{(2\omega)}| \quad (2)$$

where  $E^Q$  indicates the SH fields generated from  $\alpha$ -quartz, a reference sample in the experiment.  $A'$ ,  $A$ , and  $B$  are the geometric factors, including refractive indices at  $\omega$ ,  $2\omega$  of In<sub>2</sub>Se<sub>3</sub>, and the angle of incidence. We calculated them to extract the magnitudes of the  $\chi_{xxx}^{(2\omega)}$  and  $\chi_{zxx}^{(2\omega)}$  (see Supporting Material for details). We used the refractive index from the bulk  $\alpha$ -In<sub>2</sub>Se<sub>3</sub> to have a wide spectral range as well as to stay less sensitive to the ellipsometry fitting model. Our DFT calculation expects the

refractive indices from the bulk and a few layers to be off by less than 15 % in magnitude with similar spectral shape.

The relative magnitudes of the tensor components are consistent between the experiment and the theory. In particular, sharp increase between 1QL and 2 QL has been observed which might be related to the confinement effect in the 2D limit and the electric dipole arrangement. The tensor components on 3 QL is still larger than the others throughout the measured photon energy range by less than 20%.  $\chi_{xxx}^{(2\omega)}$  is smaller than  $\chi_{zxx}^{(2\omega)}$  in magnitude by a factor of 3 in 2 QL and 4 in 3 QL.

Since the phase difference between  $\chi_{xxx}^{(2\omega)}$  and  $\chi_{zxx}^{(2\omega)}$  could not be determined directly in the experiment, when we calculated  $\chi_{zxx}^{(2\omega)}$  from s-in/p-out SHG intensity, we calculated both *in-phase* and *out-of-phase* cases. When the two components are *in-phase*, the relative magnitudes differ by a couple of orders of magnitude, while they are in the same orders of magnitudes when *out-of-phase*. The latter case agrees with our DFT calculation and therefore, we concluded that the two components are close to *out-of-phase*.

## B. Transmission and Dielectric Functions

Fig. 3a presents the measured transmission spectra of our samples for 1–5, 7, 12, 25, and 37 QLs, over an energy range of 1.5 to 4 eV. We were unable to find a 6 QL region in the synthesized samples. At each photon energy, total sample transmission was divided by the separately measured transmission of the bare mica substrate, in order to isolate the optical response of the nanofilm. The shaded region represents the measurement uncertainty. As mentioned previously, we calculated the optical response for two representative structures (wurtzite-like and zincblende-like), along with many possible stacking arrangements that are possible for two or more QLs, including different horizontal placement between QLs (with no relative rotation), and various combinations of dipole directions for individual QLs in a stack. Our calculated transmission spectra are presented in Figure 3b for 1–3 QLs, 6 QLs, and bulk. The shaded regions around each curve correspond to the maximum and minimum values of the numerous stacking arrangements, while the solid curves represent the average value for each number of QLs. Calculations of the optical response for more than 6 QLs, or  $G_0W_0$  self-corrections on the bandgap for more than 2 QLs, were not practical due to the required computational resources. Therefore, these theoretical results have no quasiparticle correction applied to them. Calculated band structures (not shown) indicate that all stacking arrangements have indirect band gaps.

We first note that the various stacking arrangements yield calculated spectra that are quite consistent for each number of QLs. For 1–3 QLs, calculated and measured transmission differ by around 6 % over the measured spectral range. The calculated spectrum for 6 QLs also

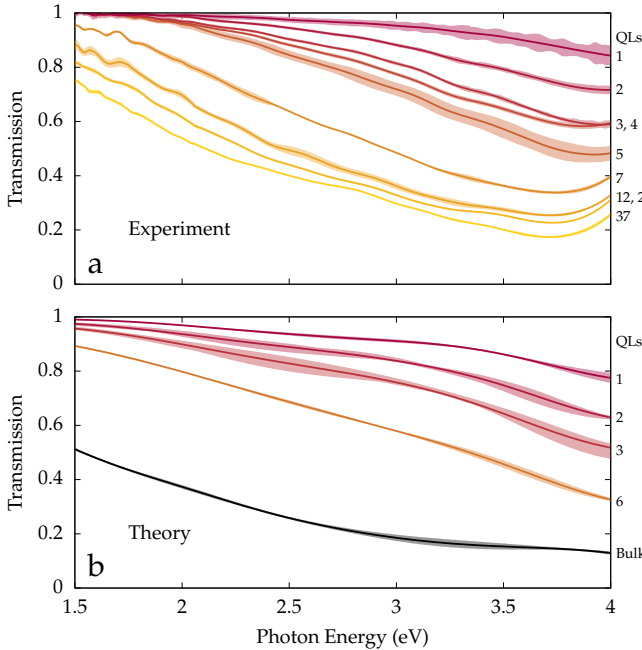


FIG. 3. **a**, experimental transmission spectra for layered  $\alpha$ -In<sub>2</sub>Se<sub>3</sub> in the range of 1.5–4 eV, for 1 to 37 QLs. **b**, theoretical results for 1–3 QLs, 6 QLs and bulk. Shaded regions around the theoretical curves represent the different stacking arrangements for any given number of QLs.

differ by less than 7 % from the average transmission of the 5 and 7 QL samples. For these cases, the calculations reproduced the observed decrease in transmission from 1.5 to 4 eV reasonably well. The experimental transmission spectra below 7 QLs are dominated by a single broad peak around 4 eV and a small shoulder around 2.5 eV. Above 7 QLs, the lower energy peak becomes more prominent, and shifts to  $\sim 2.3$  eV, while the higher energy peak shifts to  $\sim 3.7$  eV. For the calculated spectra, the lower energy peak manifests itself as a tail or shoulder in the calculated spectra. In bulk  $\alpha$ -In<sub>2</sub>Se<sub>3</sub>, it becomes a more prominent shoulder. The peak above 3.4 eV (2.5 eV) corresponds to optical transitions around the K (M) points. Thus hereafter, we will call it the K-(M-) peak. We have not applied any form of quasiparticle energy correction to the theoretical results for these layered samples. This tends to increase the calculated bandgap, which blue-shifts the dielectric function, and consequently, the calculated transmission spectra. However, even without the corrected eigen-energies, our calculations not only describe the trends in the experimental data, but are also consistent with previously reported experimental<sup>27</sup> and theoretical<sup>29</sup> results.

Fig. 4 compares the experimental (1.5–5 eV) and theoretical (0–10 eV) refractive indices for bulk  $\alpha$ -In<sub>2</sub>Se<sub>3</sub>. The scatter points are from the experimental SE fitting and the solid curves are from TDDFT calculations. We used the high spatial resolution ( $\sim 1 \mu\text{m}$ ) of the imaging ellipsometer to avoid taking data from the sample edges and

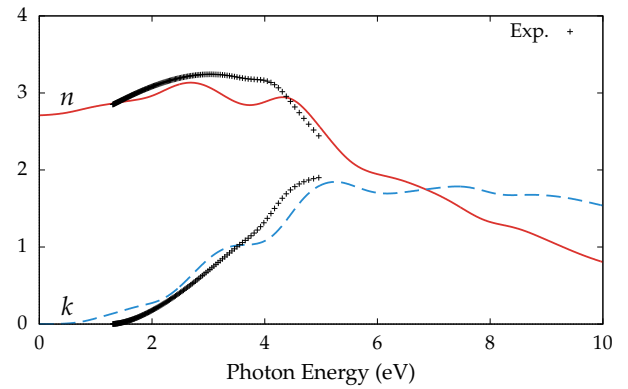


FIG. 4. The real and imaginary parts of the complex index of refraction ( $n$  and  $k$ ) for bulk  $\alpha$ -In<sub>2</sub>Se<sub>3</sub>, calculated over a photon energy range of 0–10 eV and measured in 1.5–5 eV. Theoretical curves use  $G_0W_0$  obtained quasiparticle correction for the band gap of 1.11 eV.

the adsorbed dirt from the air. To obtain the ellipsometric dielectric functions, we constructed a model using two Tauc-Lorentz oscillators. Mean-Square-Error in the fitting was less than 15. The theoretical curves in figure 4 include a quasiparticle correction of 0.66 eV, obtained from an *ab initio*  $G_0W_0$  calculation, placing the optical band gaps at 1.11 eV. This value differs by 5 % from the experimental value of 1.167 eV, and are slightly lower than previously reported values for the  $G_0W_0$  corrected optical band gap<sup>27</sup>. The calculated  $k$  spectrum has a dominant peak around 4.7 eV, with a smaller shoulder at around 3.35 eV. Although these peaks are not resolved experimentally, the measured real  $n$  (imaginary  $k$ ) differ on average by less than 15 % (30 %) throughout the measured photon energy range.

The calculated band structure (not shown) is consistent with previously reported results<sup>27</sup>, with the optical band gaps occurring around the  $\Gamma$  point. Transitions begin to accumulate rapidly around 2.5 eV (isolated around the M point). The greatest density of transitions occurs between 3.0 and 4.0 eV, primarily between the  $\Gamma$ , K, and M points. Transitions above 4.0 eV correspond to transitions between the second-highest valence band and the lowest conduction band, or between the highest valence band and the third lowest conduction band.

Although we cannot discern between the theoretical structures or between the numerous possible stacking configurations from this comparison of linear optical quantities, the overall agreement between theory and experiment is a strong indicator that the selected theoretical structures represent the atomic configuration of the real samples. The results presented above provide two important points of comparison. First, excellent agreement for the bulk optical constants, and good agreement for the dielectric functions for the layered samples both demonstrate that the intrinsic material properties are accurately portrayed by our combination of relaxed atomic coordinates and *ab initio* calculations. Second, agree-

ment between the experimental transmission curves (via direct measurement) compared with the calculated dielectric functions (within a straightforward transmission model) indicates that the intrinsic material properties are accurately matched with real experimental conditions, such as individual QL thickness.

### C. Band Gaps

Fig. 5 presents the optical band gap dependence on the number of QLs, extracted from the transmission curves for the layered samples, and ellipsometry fitting for the bulk. To obtain the error bars, we repeated the fitting on several measurements obtained from different spots on the same flake. The values decrease steadily as the number of layers increases, starting at  $\sim 2.5$  eV for 1 QL down to  $\sim 1.167$  eV for the bulk. The latter value is lower than the previously reported values ( $\sim 1.4$  eV) obtained from a transmission measurement and *ab initio*  $G_0W_0$  calculations<sup>27,54</sup>, although it is well within the range of the reported optical band gaps for  $\alpha$ -In<sub>2</sub>Se<sub>3</sub> (see Table I). Our  $G_0W_0$  calculation yields a bulk optical band gap value of 1.11 eV, which agrees within 5% of the measured optical band gap; for 1 and 2 QLs, the calculated bandgap differs by 15% of the measured values. Table I present a comprehensive summary of reported optical bandgap values, including those presented in this work. As we can see from the table, the gap values (both experimental and theoretical) span a wide range; in bulk, the optical band gap varies from 1.154 eV to 1.48 eV. However, the band gaps reported in this work are consistent with the ones available from the literature.

The motion of electrons in one or multiple QLs is confined to the direction perpendicular to the QL plane, while the carriers can move freely along the films. Such confinement of the charge carriers can be qualitatively explained considering that the In<sub>2</sub>Se<sub>3</sub> flakes act as 1D quantum wells<sup>27</sup>. In terms of the electron band structure, if the corresponding 3D layered system is semiconducting with banggap  $E_g$ , the corresponding free-standing or de-

TABLE I. The optical band gaps (in eV) presented in this work compared to values reported in the literature.

Sample	Experiment (eV)	$G_0W_0$ (eV)
1 QL	$2.597 \pm 0.130$	2.241
2 QL	$2.123 \pm 0.075$	1.820
3 QL	$1.987 \pm 0.014$	—
4 QL	$1.960 \pm 0.010$	—
5 QL	$1.963 \pm 0.013$	—
Bulk	1.167	1.110

posited 2D layers (especially on an insulating substrate) should have a larger bandgap due to this confinement effect. The largest increase in the band gap occurs when going from one to multiple QLs, as the value decreases inversely proportional to the square of the film thickness<sup>27</sup>. This simple model, which also depends on the effective mass of the electrons and holes, yield an energy decrease of 0.47 eV when going from one QL to two QLs, and a decrease of 0.14 eV between two QLs and three QLs. The gap widening in nano-thin films with decreasing thickness is clearly observed in our first principle calculations<sup>55</sup>.

## IV. CONCLUSION

We have investigated the linear and nonlinear optical response of a few layers of  $\alpha$ -In<sub>2</sub>Se<sub>3</sub>. Spectroscopic transmission and ellipsometry measurements were used to obtain the linear optical response. These two independent methods, combined with *ab initio* calculations for 1-3, 6 QL and bulk, provide a comprehensive set of optical response from single QL to bulk  $\alpha$ -In<sub>2</sub>Se<sub>3</sub>. Our calculations provide good agreement with the experimental data; in particular  $G_0W_0$  calculation yields a bandgap for the bulk that is within 10% of the experimental values. Calculated TDDFT and DFT-LDA *ab initio* dielectric functions and transmission spectra are comparable to those obtained from spectroscopic ellipsometry and transmission measurements.

From the experimental data, we analyzed two peaks around 2.5 eV and 4 eV, which correspond to optical transitions around the M- and K-points in momentum space, respectively. We have shown that changing the thickness of the material tunes the optical band gap of  $\alpha$ -In<sub>2</sub>Se<sub>3</sub> from visible (2.6 eV) to infrared (1.17 eV) photon energies, with significant absorption. The optical band gap tunability range of 1.4 eV is consistent with previous measurements for QL thicknesses between 3–25 nm<sup>27</sup> and is one of the largest amongst known 2D materials, which typically ranges  $\sim 0.5$  eV<sup>27,56</sup>. This property suggests potential applications as photodetectors<sup>38,57</sup> or as solar cell material.

Although linear optical measurements show how the dielectric functions change with photon energy and QL thickness, it is insensitive to the change in stacking

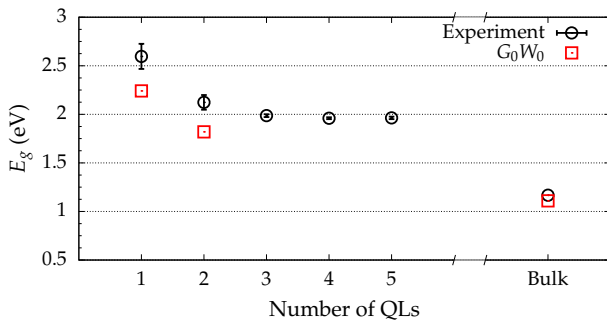


FIG. 5. The optical band gap values obtained from the experimental measurements, and the two corresponding bulk values obtained from a  $G_0W_0$  calculation.

order or net polarization, which is critical to understand ferroelectricity on a few QLs of  $\alpha$ -In<sub>2</sub>Se<sub>3</sub>. We used second-harmonic generation microscopy and spectroscopy to probe it. The SHG response peaks at 3 QL and decreases at thicker QLs, as oppose to monotonically changing linear response, indicating that 3 QL has the strongest net polarization. In addition, the horizontal stacking order significantly changes the SHG response; by rotating  $\sim 30^\circ$ , the SHG response is decreased by a factor of 3. This tunability suggests that we can fine-tune the optical response towards desired optoelectronic applications.

## V. ACKNOWLEDGMENTS

This work was supported by Robert Welch Foundation grant F-1038. Y. Cho acknowledges InProTUC (Internation-

nal Promovieren an der Technischen Universitt Chemnitz) program for supporting her research at TU Chemnitz. Sample preparation was supported by Welch Foundation Grant F-1814, and the U.S. Department of Energy (DOE), Office of Science, Basic Energy Sciences, under Awards DE-SC0010308 and DE-SC0019025. Additionally, the authors thankfully acknowledge the computer resources, technical expertise, and support provided by the Laboratorio Nacional de Supercómputo del Sureste de México, a member of the CONACYT network of national laboratories as well as the Shared Hierarchical Academic Research Computing Network (SHARCNET) of Ontario, Canada.

---

\* [sma@cio.mx](mailto:sma@cio.mx)

- <sup>1</sup> D. Boukhvalov, B. Grbulak, S. Duman, L. Wang, A. Politan, L. Caputi, G. Chiarello, and A. Cupolillo, *Nanomaterials* **7**, 372 (2017).
- <sup>2</sup> S. Demirci, N. Avazli, E. Durgun, and S. Cahangirov, *Phys. Rev. B* **95**, 115409 (2017).
- <sup>3</sup> J. Lin, Z. Fang, H. Tao, Y. Li, X. Huang, K. Ding, S. Huang, and Y. Zhang, *CrystEngComm* **20**, 2573 (2018).
- <sup>4</sup> H. Henck, D. Pierucci, J. Zribi, F. Bisti, E. Papalazarou, J.-C. Girard, J. Chaste, F. Bertran, P. Le Fèvre, F. Sirotti, L. Perfetti, C. Giorgetti, A. Shukla, J. E. Rault, and A. Ouerghi, *Phys. Rev. Mater.* **3**, 034004 (2019).
- <sup>5</sup> J.-S. Rhyee, K. H. Lee, S. M. Lee, E. Cho, S. I. Kim, E. Lee, Y. S. Kwon, J. H. Shim, and G. Kotliar, *Nature* **459**, 965 (2009).
- <sup>6</sup> G. Han, Z.-G. Chen, C. Sun, L. Yang, L. Cheng, Z. Li, W. Lu, Z. M. Gibbs, G. J. Snyder, K. Jack, J. Drennan, and J. Zou, *CrystEngComm* **16**, 393 (2014).
- <sup>7</sup> L. Debbichi, O. Eriksson, and S. Lebègue, *Ann. Phys.* **526**, 402 (2014).
- <sup>8</sup> D. A. Bandurin, A. V. Tyurnina, G. L. Yu, A. Mishchenko, V. Zólyomi, S. V. Morozov, R. K. Kumar, R. V. Gorbatchev, Z. R. Kudrynskyi, S. Pezzini, Z. D. Kovalyuk, U. Zeitler, K. S. Novoselov, A. Patané, L. Eaves, I. V. Grigorieva, V. I. Fal'ko, A. K. Geim, and Y. Cao, *Nat. Nanotechnol.* **12**, 223 (2016).
- <sup>9</sup> G. Liu, K. Chen, and J. Li, *J. Am. Ceram. Soc.* **101**, 36 (2018).
- <sup>10</sup> W. Ding, J. Zhu, Z. Wang, Y. Gao, D. Xiao, Y. Gu, Z. Zhang, and W. Zhu, *Nat. Commun.* **8**, 14956 (2017).
- <sup>11</sup> J. F. Scott, *Science* **315**, 954 (2007).
- <sup>12</sup> S. L. Miller and P. J. McWhorter, *J. Appl. Phys.* **72**, 5999 (1992).
- <sup>13</sup> B. H. Park, B. S. Kang, S. D. Bu, T. W. Noh, J. Lee, and W. Jo, *Nature* **401**, 682 (1999).
- <sup>14</sup> S. Wan, Y. Li, W. Li, X. Mao, W. Zhu, and H. Zeng, *Nanoscale* **10**, 14885 (2018).
- <sup>15</sup> P. Ponath, K. Fredrickson, A. B. Posadas, Y. Ren, X. Wu, R. K. Vasudevan, M. B. Okatan, S. Jesse, T. Aoki, M. R. McCartney, D. J. Smith, S. V. Kalinin, K. Lai, and A. A. Demkov, *Nat. Commun.* **6**, 6067 (2015).
- <sup>16</sup> Y. Cho, P. Ponath, L. Zheng, B. Hatanpaa, K. Lai, A. A. Demkov, and M. C. Downer, *Appl. Phys. Lett.* **112**, 162901 (2017).
- <sup>17</sup> D. D. Fong, G. B. Stephenson, S. K. Streiffer, J. A. Eastman, O. Auciello, P. H. Fuoss, and C. Thompson, *Science* **304**, 1650 (2004).
- <sup>18</sup> B. Meyer and D. Vanderbilt, *Phys. Rev. B* **63**, 205426 (2001).
- <sup>19</sup> M.-G. Han, M. S. J. Marshall, L. Wu, M. A. Schofield, T. Aoki, R. Tweten, J. Hoffman, F. J. Walker, C. H. Ahn, and Z. Y., *Nat. Commun.* **5**, 4693 (2014).
- <sup>20</sup> M. Dawber, K. M. Rabe, and J. F. Scott, *Rev. Mod. Phys.* **77**, 1083 (2005).
- <sup>21</sup> K. Chang, J. Liu, H. Lin, N. Wang, K. Zhao, A. Zhang, F. Jin, Y. Zhong, X. Hu, W. Duan, Q. Zhang, L. Fu, Q.-K. Xue, X. Chen, and S.-H. Ji, *Science* **353**, 274 (2016).
- <sup>22</sup> S. N. Shirodkar and U. V. Waghmare, *Phys. Rev. Lett.* **112**, 157601 (2014).
- <sup>23</sup> M. Wu and X. C. Zeng, *Nano Lett.* **16**, 3236 (2016).
- <sup>24</sup> W. Li, F. P. Sabino, F. Crasto de Lima, T. Wang, R. H. Miwa, and A. Janotti, *Phys. Rev. B* **98**, 165134 (2018).
- <sup>25</sup> S. Wan, Y. Li, W. Li, X. Mao, C. Wang, C. Chen, J. Dong, A. Nie, J. Xiang, Z. Liu, W. Zhu, and H. Zeng, *Adv. Funct. Mater.* **1808606** (2019).
- <sup>26</sup> Z. Yang and J. Hao, *Adv. Mater. Technol.* **4**, 1900108 (2019).
- <sup>27</sup> J. Quereda, R. Biele, G. Rubio-Bollinger, N. Agrait, R. D'Agosta, and A. Castellanos-Gomez, *Adv. Opt. Mater.* **4**, 1939 (2016).
- <sup>28</sup> D. Wu, A. J. Pak, Y. Liu, Y. Zhou, X. Wu, Y. Zhu, M. Lin, Y. Han, Y. Ren, H. Peng, Y.-H. Tsai, G. S. Hwang, and K. Lai, *Nano Lett.* **15**, 8136 (2015).
- <sup>29</sup> L. Hu and X. Huang, *RSC Adv.* **7**, 55034 (2017).
- <sup>30</sup> X. Tao and Y. Gu, *Nano Lett.* **13**, 3501 (2013).
- <sup>31</sup> B. Yu, S. Ju, X. Sun, G. Ng, T. D. Nguyen, M. Meyyappan, and D. B. Janes, *Appl. Phys. Lett.* **91**, 133119 (2007).
- <sup>32</sup> M. S. Choi, B. Cheong, C. H. Ra, S. Lee, J.-H. Bae, S. Lee, G.-D. Lee, C.-W. Yang, J. Hone, and W. J. Yoo, *Adv. Mater.* **29**, 1703568 (2017).

<sup>33</sup> Y. Zhou, D. Wu, Y. Zhu, Y. Cho, Q. He, X. Yang, K. Herrera, Z. Chu, Y. Han, M. C. Downer, H. Peng, and K. Lai, *Nano Lett.* **17**, 5508 (2017).

<sup>34</sup> J. Xiao, H. Zhu, Y. Wang, W. Feng, Y. Hu, A. Dasgupta, Y. Han, Y. Wang, D. A. Muller, L. W. Martin, P. Hu, and X. Zhang, *Phys. Rev. Lett.* **120** (2018), 10.1103/PhysRevLett.120.227601.

<sup>35</sup> F. Xue, W. Hu, K.-C. Lee, L.-S. Lu, J. Zhang, H.-L. Tang, A. Han, W.-T. Hsu, S. Tu, W.-H. Chang, C.-H. Lien, J.-H. He, Z. Zhang, L.-J. Li, and X. Zhang, *Adv. Funct. Mater.* **28**, 1803738 (2018).

<sup>36</sup> C. Zheng, L. Yu, L. Zhu, J. L. Collins, D. Kim, Y. Lou, C. Xu, M. Li, Z. Wei, Y. Zhang, M. T. Edmonds, S. Li, J. Seidel, Y. Zhu, J. Z. Liu, W.-X. Tang, and M. S. Fuhrer, *Sci. Adv.* **4**, 8 (2018).

<sup>37</sup> M. Lin, D. Wu, Y. Zhou, W. Huang, W. Jiang, W. Zheng, S. Zhao, C. Jin, Y. Guo, H. Peng, and Z. Liu, *J. Am. Chem. Soc.* **135**, 13274 (2013).

<sup>38</sup> W. Zheng, T. Xie, Y. Zhou, Y. L. Chen, W. Jiang, S. Zhao, J. Wu, Y. Jing, Y. Wu, G. Chen, Y. Guo, J. Yin, S. Huang, H. Q. Xu, Z. Liu, and H. Peng, *Nat. Commun.* **6**, 6972 (2015).

<sup>39</sup> P. Giannozzi, O. Andreussi, T. Brumme, O. Bunau, M. Buongiorno Nardelli, M. Calandra, R. Car, C. Cavazzoni, D. Ceresoli, M. Cococcioni, N. Colonna, I. Carnimeo, A. Dal Corso, S. de Gironcoli, P. Delugas, R. A. DiStasio, A. Ferretti, A. Floris, G. Fratesi, G. Fugallo, R. Gebauer, U. Gerstmann, F. Giustino, T. Gorni, J. Jia, M. Kawamura, H.-Y. Ko, A. Kokalj, E. Küçükbenli, M. Lazzeri, M. Marsili, N. Marzari, F. Mauri, N. L. Nguyen, H.-V. Nguyen, A. Otero-de-la Roza, L. Paulatto, S. Poncé, D. Rocca, R. Sabatini, B. Santra, M. Schlipf, A. P. Seitsonen, A. Smogunov, I. Timrov, T. Thonhauser, P. Umari, N. Vast, X. Wu, and S. Baroni, *J. Phys. Condens. Matter* **29**, 465901 (2017).

<sup>40</sup> B. S. Mendoza, S. M. Anderson, J. L. Cabellos, and T. Rangel, “TINIBA: *Ab initio* calculation of the optical properties of solids, surfaces, interfaces, and 2D materials,” INDAUTOR-Mexico No. 03-2009-120114033400-01.

<sup>41</sup> S. M. Anderson, N. Tancogne-Dejean, B. S. Mendoza, and V. Véniard, *Phys. Rev. B* **91**, 075302 (2015).

<sup>42</sup> X. Gonze, B. Amadon, P.-M. Anglade, J.-M. Beuken, F. Bottin, P. Boulanger, F. Bruneval, D. Caliste, R. Caracas, M. Côté, T. Deutsch, L. Genovese, P. Ghosez, M. Giantomassi, S. Goedecker, D. R. Hamann, P. Hermet, F. Jollet, G. Jomard, S. Leroux, M. Mancini, S. Mazevedt, M. J. T. Oliveira, G. Onida, Y. Pouillon, T. Rangel, G.-M. Rignanese, D. Sangalli, R. Shaltaf, M. Torrent, M. J. Verstraete, G. Zerah, and J. W. Zwanziger, *Comp. Phys. Commun.* **180**, 2582 (2009).

<sup>43</sup> The ABINIT code is a common project of the Université Catholique de Louvain, Corning Incorporated, and other contributors (URL <http://www.abinit.org>).

<sup>44</sup> N. Troullier and J. L. Martins, *Phys. Rev. B* **43**, 1993 (1991).

<sup>45</sup> V. Olevano, L. Reining, and F. Sottile, <http://dp-code.org>.

<sup>46</sup> L. Reining, V. Olevano, F. Sottile, S. Albrecht, and G. Onida, <http://www.bethe-salpeter.org>.

<sup>47</sup> N. Tancogne-Dejean, C. Giorgetti, and V. Véniard, *Phys. Rev. B* **92**, 245308 (2015).

<sup>48</sup> L. Hedin, *Phys. Rev.* **139**, A796 (1965).

<sup>49</sup> R. Boyd, *Nonlinear Optics* (Academic Press, New York, 2003).

<sup>50</sup> S. V. Popov, Y. P. Svirko, and N. I. Zheludev, *Susceptibility tensors for nonlinear optics* (CRC Press, 1995).

<sup>51</sup> J. E. Sipe, D. J. Moss, and H. M. van Driel, *Phys. Rev. B* **35**, 1129 (1987).

<sup>52</sup> C. Yamada and T. Kimura, *Phys. Rev. B* **49**, 14372 (1994).

<sup>53</sup> G. Plechinger, F. Mooshammer, A. Castellanos-Gomez, G. A. Steele, C. Schüller, and T. Korn, *2D Materials* **2**, 034016 (2015).

<sup>54</sup> L. Debbichi, O. Eriksson, and S. Lebégue, *J. Phys. Chem. Lett.* **6**, 3098 (2015).

<sup>55</sup> A. I. Shkrebtii, R. Minnings, G. Perinparajah, N. Arzate, S. Anderson, B. Mendoza, Y. Cho, M. Downer, and D. Zahn, in *ANM 2019: Advanced Nano Materials Conference* (Aveiro, Portugal, 2019) to be submitted to proceedings on Sep 30.

<sup>56</sup> J. Gusakova, X. Wang, L. L. Shiau, A. Krivosheeva, V. Shaposhnikov, V. Borisenko, V. Gusakov, and B. K. Tay, *Phys. Status Solidi A* **214**, 1700218 (2017).

<sup>57</sup> Z. Q. Zheng, J. D. Yao, and G. W. Yang, *J. Mater. Chem. C* **4**, 8094 (2016).